

## Onset of midvelocity emissions in symmetric heavy ion reactions

E. Plagnol,<sup>2</sup> J. Łukasik,<sup>2,\*</sup> G. Auger,<sup>1</sup> Ch. O. Bacri,<sup>2</sup> N. Bellaïze,<sup>3</sup> F. Bocage,<sup>3</sup> B. Borderie,<sup>2</sup> R. Bougault,<sup>3</sup> R. Brou,<sup>3</sup> P. Buchet,<sup>4</sup> J. L. Charvet,<sup>4</sup> A. Chbihi,<sup>1</sup> J. Colin,<sup>3</sup> D. Cussol,<sup>3</sup> R. Dayras,<sup>4</sup> A. Demeyer,<sup>5</sup> D. Doré,<sup>4</sup> D. Durand,<sup>3</sup> J. D. Frankland,<sup>2</sup> E. Galichet,<sup>5</sup> E. Genouin-Duhamel,<sup>3</sup> E. Gerlic,<sup>5</sup> D. Guinet,<sup>5</sup> P. Laitesse,<sup>5</sup> J. L. Laville,<sup>1</sup> J. F. Lecolley,<sup>3</sup> R. Legrain,<sup>4</sup> N. Le Neindre,<sup>3</sup> O. Lopez,<sup>3</sup> M. Louvel,<sup>3</sup> A. M. Maskay,<sup>5</sup> L. Nalpas,<sup>4</sup> A. D. Nguyen,<sup>3</sup> M. Pârlog,<sup>6</sup> J. Péter,<sup>3</sup> M. F. Rivet,<sup>2</sup> E. Rosato,<sup>7</sup> F. Saint-Laurent,<sup>1,†</sup> S. Salou,<sup>1</sup> J. C. Steckmeyer,<sup>3</sup> M. Stern,<sup>5</sup> G. Tăbăcaru,<sup>6</sup> B. Tamain,<sup>3</sup> L. Tassan-Got,<sup>2</sup> O. Tirel,<sup>1</sup> E. Vient,<sup>3</sup> C. Volant,<sup>4</sup> and J. P. Wieleczko<sup>1</sup>

(The INDRA Collaboration)

<sup>1</sup>GANIL, CEA et IN2P3–CNRS, Boîte Postale 5027, F-14076 Caen Cedex, France

<sup>2</sup>Institut de Physique Nucléaire, IN2P3–CNRS, F-91406 Orsay Cedex, France

<sup>3</sup>LPC, IN2P3–CNRS, ISMRA et Université, F-14050 Caen Cedex, France

<sup>4</sup>DAPNIA/SPhN, CEA/Saclay, F-91191 Gif sur Yvette Cedex, France

<sup>5</sup>Institut de Physique Nucléaire, IN2P3–CNRS et Université, F-69622 Villeurbanne Cedex, France

<sup>6</sup>National Institute for Physics and Nuclear Engineering, RO-76900 Bucharest-Măgurele, Romania

<sup>7</sup>Dipartimento di Scienze Fisiche e Sezione INFN, Università di Napoli “Federico II,” I-80126 Napoli, Italy

(Received 28 May 1999; published 20 December 1999)

Experimental data obtained with the  $4\pi$  multidetector system INDRA are used to study midvelocity emissions of light charged particles (LCP) and intermediate mass fragments for peripheral and semicentral collisions of Xe and Sn at energies between 25 and 50 MeV/nucleon. The analysis is performed as a function of incident energy and of impact parameter, defined through the total transverse energy of LCP. The onset of midvelocity emissions is found to be close to 25 MeV/nucleon. Evaporative processes are also identified and are found to be sensitive to the impact parameter but show, for a given impact parameter, little dependence on the incident energy. A chemical analysis of the midvelocity component is performed. Compared to the evaporative process, midvelocity matter is found to be more neutron rich. Results are compared with the predictions of a dynamical model (CHIMERA). The general trends are well reproduced but some interesting differences are observed, notably in the amount of relative energy dissipation, showing that midvelocity emissions could be sensitive to the finer details of the interaction.

PACS number(s): 25.70.Mn, 25.70.Lm, 25.70.Pq

### I. INTRODUCTION

The study of nuclear reactions in the Fermi energy domain (30–50 MeV/nucleon) and the proper understanding of mechanisms by which the two interacting nuclei (projectile and target) exchange mass, charge, and energy, and eventually fuse, is one of the major goals of nuclear physics. At low energies ( $\leq 20$  MeV/nucleon) and for noncentral collisions the process is essentially a binary one where energy dissipation and mass transfer are explained by nucleon exchange models [1]. At these energies and for central collisions, a fusion process is observed for light systems. At relativistic energies ( $\geq 300$  MeV/nucleon) the collisions are explained within the participant-spectator model (fireball) where the overlap region (participant) between the projectile and the target decouples from the spectators.

It is only quite recently that experimental data [2–10] have given indications of the transition from one regime to the other. This appears as a production of both light particles

and heavier fragments with parallel velocities intermediate between those of the projectile and of the target. These emissions appear to be strongly influenced by dynamical effects and are thought to proceed on a relatively short time scale. They are called midvelocity emissions, dynamical emissions, or intermediate velocity products.

An important source of particle and fragment production remains of course the statistical evaporative process from the excited quasiprojectile and quasitarget. For most of the cross section (i.e., the larger impact parameters) their lifetimes are long enough that these processes take place once the different sources are well separated. The midvelocity emissions can therefore be defined by opposition to these processes. They will therefore include a variety of mechanisms: fast pre-equilibrium particles, neck emitted particles and fragments, as well as light fission fragments preferentially aligned in between the two main reaction partners (see Sec. V).

In a preceding paper Łukasik *et al.* [8] have studied these emissions for the Xe+Sn at 50 MeV/nucleon and have found that, at this energy, they correspond to a significant part of the total charge: up to 30% for midperipheral collisions ( $b \sim 5$  fm). The object of the present work is to study these productions as a function of the projectile energy and to establish at what energies they appear.

\*Permanent address: Institute of Nuclear Physics, ul. Radzikowskiego 152, 31-342 Kraków, Poland.

†Present address: DRFC/STEP, CEA/Cadarache, F-13018 Saint-Paul-lez-Durance Cedex, France.

Section II presents the experimental procedure and Sec. III the impact parameter sorting method that has been used. In Secs. IV and V a detailed analysis of the size and chemical composition of these emissions is given. Section VI will compare the data to the prediction of a dynamical model.

## II. EXPERIMENTAL PROCEDURE

The experiment was performed at the GANIL accelerator with the INDRA detector. The detector can be schematically described as a set of 17 detection rings centered on the beam axis. The most forward ring ( $2^\circ \leq \theta_{\text{lab}} \leq 3^\circ$ ) is made of phoswich detectors: NE102(0.5 mm)+NE115(25 cm). From  $3^\circ$  to  $45^\circ$ , rings are made of three detection layers: ionization chambers (5 cm of  $C_3F_8$  at 30 mbar), silicon (300  $\mu\text{m}$ ), and CsI (13.8 to 9 cm). Beyond  $45^\circ$ , the remaining eight rings have double detection layers: ionization chambers (5 cm of  $C_3F_8$  at 20 mbar) and CsI (7.6 to 5 cm). The total number of detection cells is 336. In the forward region ( $3^\circ \leq \theta_{\text{lab}} \leq 45^\circ$ ), ions with  $Z$  up to 54 are identified if their energies are greater than the Bragg peak value. Below this energy, only a minimum  $Z$  value can be attributed. Beyond  $45^\circ$ , a proper identification is obtained up to  $Z=16$ , and for higher  $Z$  the uncertainty is estimated to be of the order of 2 to 3 units. Over the whole angular range, a very good isotope identification is obtained for  $Z=1$  to  $Z=3$ , except for particles with low laboratory energies where ambiguities are unresolved. Computer simulations of both the detector efficiency and the identification and energy calibration processes show that a good understanding of the functioning of the detector is achieved. A complete technical description of the detector and of its electronics can be found in [11].

In order for the detector to function in the best conditions and to keep random coincidences down (below  $10^{-4}$ ), a beam current of  $5.0 \times 10^7$  incident Xe ions per second was used. The target was made of natural Sn with a thickness of  $350 \mu\text{g}/\text{cm}^2$ . A minimal bias trigger was used that registered all the events with at least four detectors fired. The data was collected at energies of 25, 32, 39, 45, and 50 MeV/nucleon.

The absolute cross sections are calculated by using the target thickness and the measure of the integrated beam charge. At 45 MeV/nucleon a malfunction of the beam integrator has resulted in abnormal values of the total cross section. For this reason, the values used at this energy correspond to an interpolation between the values at the other energies (see inset of Fig. 2).

## III. IMPACT PARAMETER SORTING

The participant spectator model, valid at high energies, is essentially a geometrical model. In order to evaluate geometrical effects in the Fermi energy domain, it is essential to use an impact parameter ( $b$ ) sorting procedure. This type of sorting also allows an instructive comparison of the data and hence of different production mechanisms at different incident energies for specific impact parameter ranges.

As previously [8], we have chosen the Etrans12, transverse energy of light charged particles (LCP,  $Z=1,2$ ), as an impact parameter selector. This observable is quite well cor-

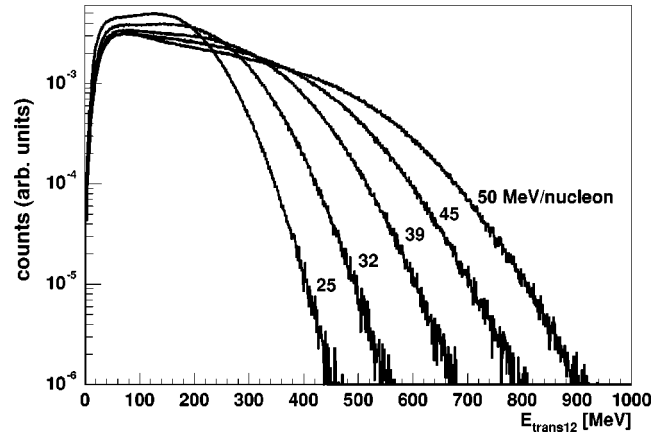


FIG. 1. Distribution of transverse energy of light charged particles (Etrans12) for 25, 32, 39, 45, and 50 MeV/nucleon Xe+Sn.

related with the impact parameter, especially for peripheral and midcentral collisions, and well suited to the data because the INDRA detector is very efficient ( $\sim 85\%$ ) for LCP's. The exact correlation between  $b$  and the value of Etrans12, and its fluctuations will be discussed in Sec. VI.

Figure 1 presents normalized Etrans12 spectra for 25, 32, 39, 45, and 50 MeV/nucleon incident energies. The observed low Etrans12 threshold is associated with an "offline" requirement for charged product multiplicities  $\geq 4$ , in order to be consistent with the data acquisition trigger which was sensitive to neutrons, gammas, and electrons. These spectra are used to find the relationship between Etrans12 and the impact parameter. This is done with the use of the following geometrical prescription [12]:

$$b(\text{Etrans12}) = b_{\text{max}} \cdot \left( \frac{\int_{\text{Etrans12}}^{\infty} \text{spectrum}(\text{Etrans12})}{\int_0^{\infty} \text{spectrum}(\text{Etrans12})} \right)^{1/2}.$$

In order to compare the shapes obtained at different energies, the Etrans12 values are scaled proportionally to the incident energy, i.e., by the factor  $50/(\text{energy/nucleon})$ . Thus the scaled Etrans12 for 50 MeV/nucleon is just the original Etrans12, and the Etrans12 scale for the remaining incident energies is appropriately stretched. Figure 2 shows the results of this procedure applied to the Etrans12 spectra for all incident energies.

For each spectrum the value of Etrans12 corresponding to 5% of the  $b_{\text{max}}$  is extracted (bin 8). Below this value of Etrans12 the spectrum is further divided into seven equal bins. The most peripheral events correspond therefore to bin 1 and the most central to bin 8. This binning is indicated by black circles with numbers below the  $x$  axis. As can be seen, this binning procedure produces almost equivalent impact parameter bins for all incident energies. These impact parameter bins are correspondingly labeled with the white circles with numbers on the  $y$  axis.

The knowledge of the absolute value of the total cross sections allows us to express  $b$  in fm. Notice that the total cross sections measured in this work correspond to events

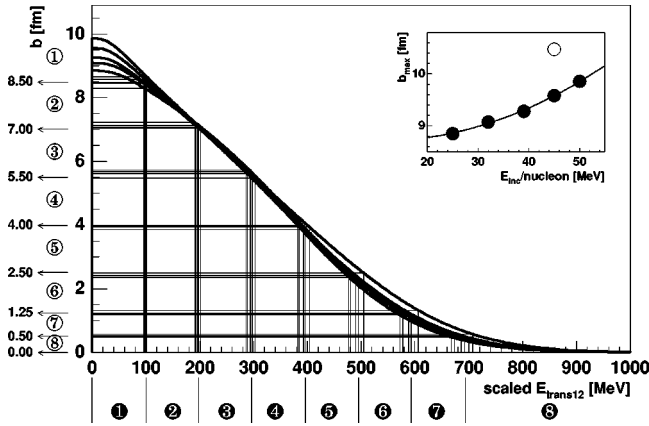


FIG. 2. Relationship between scaled Etrans12 and impact parameter ( $b$ ) for all incident energies, obtained with the use of the geometrical prescription defined in Sec. III. Scaled Etrans12 = Etrans12\*[50/(Einc/nucleon)]. The black circles with numbers along the abscissa denote respective Etrans12 bin numbers, used later on to identify the Etrans12 bins. The corresponding impact parameter bins are labeled with white circles with numbers along the ordinate. Bin 1 selects the most peripheral events and bin 8 corresponds to the most central ones. The solid circles in the inset, except the point for 45 MeV/nucleon, represent the  $b_{\max}$  derived from experimental cross sections. The value for 45 MeV/nucleon is the interpolated one. The open circle represents the original experimental  $b_{\max}$  value for 45 MeV/nucleon.

with at least four charged products detected. The values of the  $b_{\max}$ 's can be read out for Etrans12=0 or from the inset. As might be expected, the  $b_{\max}$ 's decrease with the decreasing incident energy, since the lower the incident energy, the more violent the collision needed to produce at least four charged fragments.

Comparison with values given in Ref. [8] shows a smaller value of  $b_{\max}$  at 50 MeV/nucleon (from 10.7 to 9.81) due to a correction in the data analysis.

#### IV. STUDY OF MIDVELOCITY AND EVAPORATIVE EMISSIONS AS A FUNCTION OF INCIDENT ENERGY

In order to trace the evolution of the midvelocity emissions with the incident energy a momentum tensor analysis [13] is performed and the subtraction method described in [8] is used and applied to the forward hemisphere (i.e., the projectile side) in the frame of the principal axis of the momentum tensor. This method requires the knowledge of the velocity of the evaporative source of particles and fragments. Knowing this source velocity and assuming an isotropic statistical emission pattern in the source frame, the midvelocity component is extracted by doubling the forward yield with respect to the source, and subtracting it from the total yield in the forward hemisphere in the frame of the principal axis of the momentum tensor. It is important to note that the method can be applied only if a significant fraction of the total charge is detected: only events where the total charge detected was equal to or greater than that of the quasiprojectile have been analyzed. When necessary, the missing quasi-

target was deduced by charge and energy conservation.

A key problem of this analysis is the knowledge of the evaporative source velocity. Two different methods are used to estimate this quantity.

Method I assumes that the most probable velocity of the heaviest fragments detected in a sample of events for a given impact parameter bin is a reasonable estimate for the mean source velocity of that sample. It is clear that for central collisions this method loses its accuracy for at least two reasons. First, for the more central collisions the separation between the two sources is debatable, especially at lower energies. Secondly, even if the two source picture is still valid, the heaviest fragment is not systematically related to the projectile remnant as it is assumed. This will normally lead to an overestimation of the quasiprojectile source size.

Method II utilizes the thrust concept [13,14]. In this method one attributes all the fragments ( $Z \geq 3$ ) to two (projectile- and targetlike) sources (PLS and TLS) in a way that maximizes the "thrust" value:

$$T = \max \frac{\left| \sum_{i \in \text{PLS}} \vec{p}_i \right| + \left| \sum_{j \in \text{TLS}} \vec{p}_j \right|}{\sum_{k \in \text{PLS} \cup \text{TLS}} |\vec{p}_k|}$$

Here, in turn, the method by definition has a tendency to diminish the source velocity, since it takes into account the slow midvelocity fragments and will therefore tend to underestimate the midvelocity component.

Both methods are quite schematic and can only yield estimates of the studied processes. Large fluctuations around the mean values are inherent in both methods and the associated errors are very difficult to estimate. The difference between the two different methods reflects the associated sensitivity and hence gives an idea of the uncertainty of these procedures. It is however possible that the exact values lie beyond these two estimations. It is shown for example by some dynamical codes [15], that even the forward hemisphere can be contaminated by energetic midvelocity emissions.

Both methods fail for central collisions, mainly because two distinct and separated sources (quasiprojectile and quasitarget) are assumed. The corresponding results for the smaller impact parameters should be taken with great care and this is indicated by the dashed lines in the two following figures. Most probably, the values given for central collisions are unphysical. The *turnovers* observed for the midvelocity emissions are also doubtful.

The velocities of the heavy fragments are also influenced by the assumption concerning their masses. In this analysis we use the EPAX formula [16] for the relationship between the atomic and mass numbers of the fragments in vicinity of the projectile and the target. The EPAX masses are slightly smaller than the ones from the beta stability valley, and imply a larger number of free neutrons. This seems to assure a better total energy conservation. Smaller masses induce also slightly higher velocities of the heaviest fragments, and con-

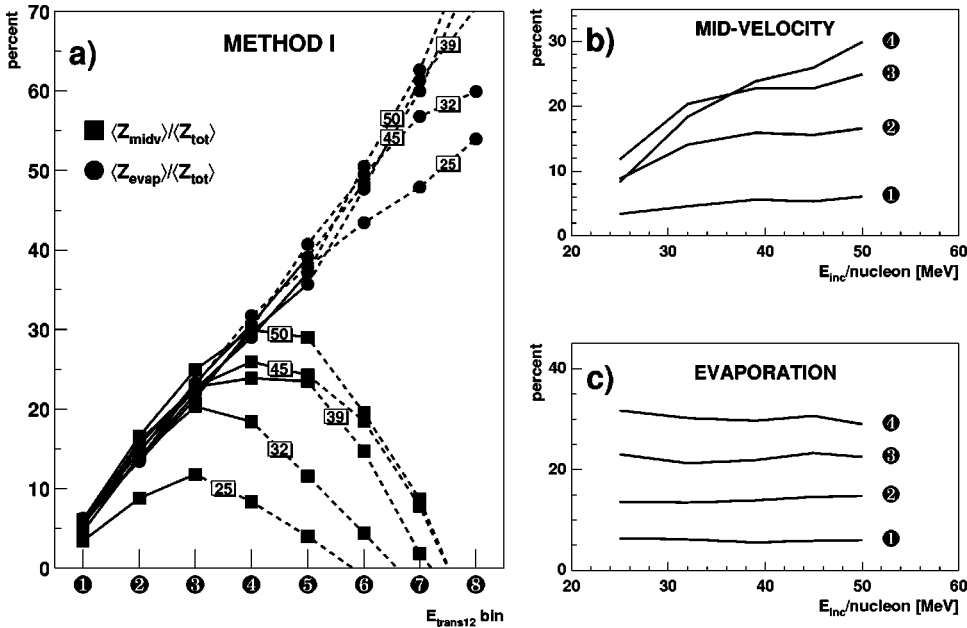


FIG. 3. (a) The percentage of charge emitted in the forward hemiellipsoid of momentum tensor for midvelocity emissions (squares) and evaporation processes (circles) obtained with method I for 8 Etrans12 bins.  $Z_{tot} = Z_{midv} + Z_{evap} + Z_{heaviest}$ . The numbers in boxes label the incident energies. The dashed lines specify the Etrans12 region for which the subtraction method described in the text gives unreliable results. (b) The percentage of charge in midvelocity component as a function of incident energy for the four most peripheral Etrans12 bins. (c) Same as (b) but for statistical emission.

sequently slightly larger midvelocity components. This can be checked by comparing Figs. 3 and 4(a) with the corresponding ones from Ref. [8].

Figures 3 and 4 present, for methods I and II, the size of the midvelocity and evaporative components for all the incident energies in percent of the mean total detected charge in the forward hemisphere ( $Z_{tot} = 53 - 50$ , from bins 1 to 4). The square symbols represent the amount of charge contained in the midvelocity component, while the circles give the information concerning the evaporated charge. In this representation, the largest fragment is not associated with either of the above processes. For this reason, the sum of the two processes *does not* add up to 100%, the difference corresponding to the charge of the largest fragment. The numbers given measure therefore *the amount of charge removed* from the quasiprojectile by either of these two modes.

The evolution of these components with the incident energy is also presented. The dashed lines represent the region of impact parameters for which both methods give unreliable results. This is the region where the two source picture is unclear, the fluctuations grow considerably, and extraction of the midvelocity component is very doubtful. It should therefore be understood that the bending over of the midvelocity fraction is probably an artifact of the method used and not necessarily an effective reduction of this process. Table I gives the velocities of the quasiprojectile source along the longest principal ellipsoide axis for the two methods in the center of mass and in units of  $c$ .

Two important conclusions can be drawn from these figures. First, panel (b) of Figs. 3 and 4 show clearly that the midvelocity component evolves from very small values at 25 MeV/nucleon incident energy (around 7–12 % of the total

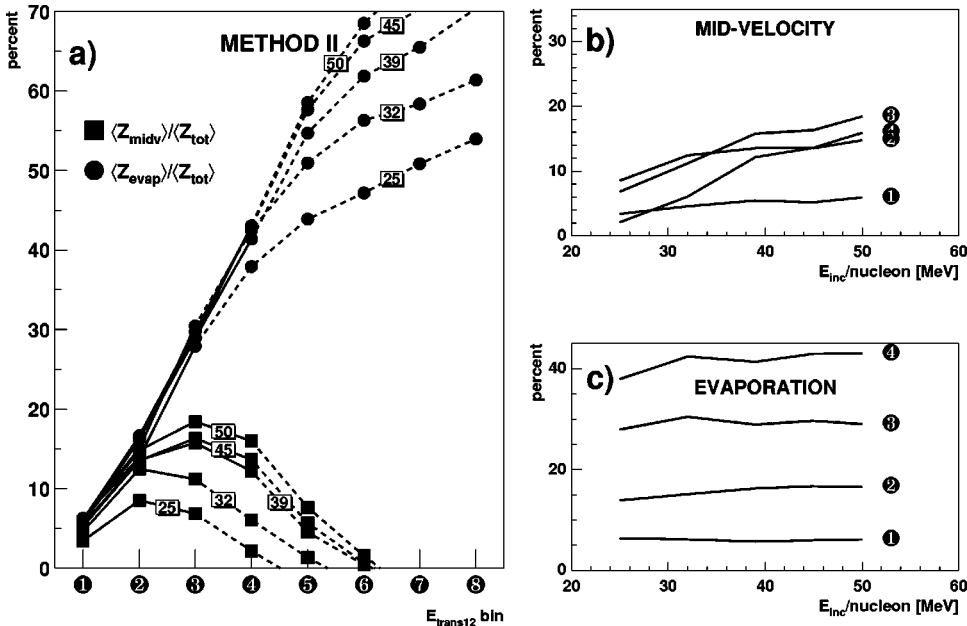


FIG. 4. Same as Fig. 3, but for method II.

TABLE I. Velocities of the quasiprojectile source for methods I and II along the principal ellipsoide axis, in the center of mass, and in units of  $c$ .

$E/A$	Velocity of quasiprojectile source (units of $c$ , in the center of mass)															
	Method 1 Bin number								Method 2 Bin number							
	1	2	3	4	5	6	7	8	1	2	3	4	5	6	7	8
25	0.103	0.097	0.088	0.077	0.069	0.061	0.055	0.046	0.103	0.096	0.077	0.066	0.059	0.055	0.050	0.046
32	0.119	0.116	0.109	0.097	0.082	0.070	0.060	0.055	0.119	0.110	0.089	0.076	0.067	0.061	0.058	0.053
39	0.131	0.126	0.120	0.111	0.103	0.086	0.068	0.057	0.130	0.117	0.104	0.091	0.076	0.068	0.063	0.057
45	0.139	0.135	0.129	0.121	0.109	0.095	0.079	0.060	0.138	0.127	0.114	0.100	0.083	0.073	0.067	0.058
50	0.151	0.144	0.139	0.132	0.119	0.099	0.082	0.062	0.149	0.137	0.124	0.108	0.089	0.077	0.068	0.065

charge) to significant proportions at 50 MeV/nucleon (up to 18–30%). The onset of midvelocity emissions is therefore *clearly observed* in this energy range.

It can also be noticed that the values of this component obtained with method I are, at 50 MeV/nucleon, already quite close to the percentage of charge that can be calculated from the geometrical overlap of the projectile and target for the corresponding impact parameters. For example, 30% is extracted for bin 4, to be compared to 33% for the geometrical overlap calculation. Measurements at higher energies should say if these values continue to rise or if a geometrical saturation is already achieved at this surprisingly low energy. Similar effects are also observed in the analysis of Ar+Ni between 52 and 95 MeV/nucleon [17].

Secondly, a surprising observation can be made concerning the evolution of the evaporative component [panel (c), in both figures]: For a given impact parameter, this component is observed to be *insensitive to the incident energy*. To our knowledge, it is possibly the first time that such a feature has been observed. This was made possible because of the  $4\pi$  coverage of the detector and because of the impact parameter measurement. Coupled to the previous observation of the onset of midvelocity emissions, the implication of this fea-

ture on the excitation energy of the evaporative source has to be studied in more detail. This will be attempted in Sec. VI.

## V. CHEMICAL COMPOSITION OF THE MIDVELOCITY AND EVAPORATIVE COMPONENTS

The upper row of Fig. 5 presents the mean multiplicities of LCP's (dashed line) and IMF's (solid line) of the midvelocity (squares) and evaporative (circles) components for method I, and for the four most peripheral impact parameter bins.

Since our analysis is restricted to the forward momentum ellipsoid hemisphere (the PLS side) and since the system is nearly symmetric, the “forward” value of these multiplicities are extrapolated to the whole system. This was done by multiplying the “forward” value by the charge ratio (104/54) of the total system to the projectile.

The mean multiplicities presented in this figure result from this extrapolation. Again, it can be noticed that not only the mean charge but also the mean multiplicity of both the evaporated LCP's and intermediate mass fragments (IMF's, defined as those with  $Z \geq 3$ , excluding the heaviest), depends very weakly on the incident energy (see circles). Whereas the

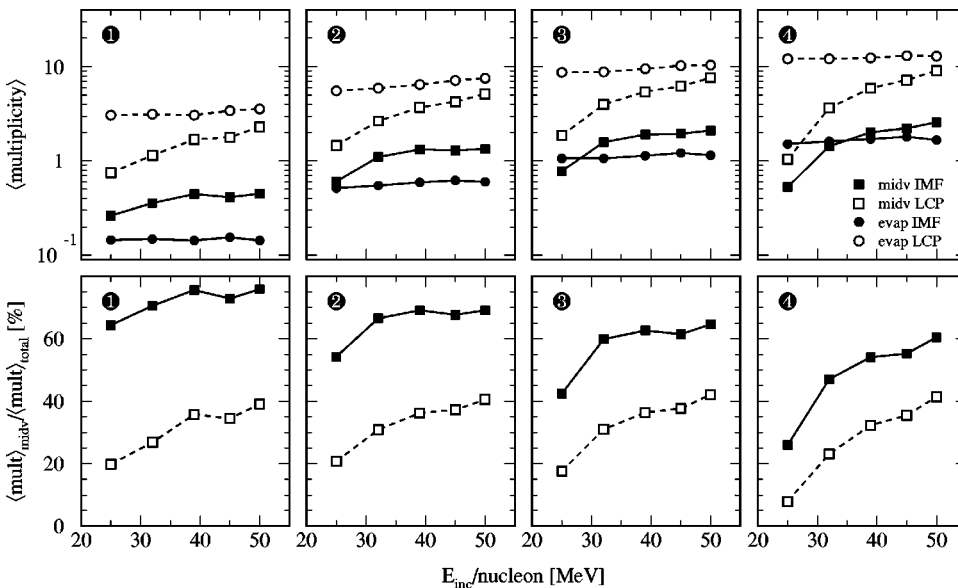


FIG. 5. Upper row: mean multiplicities of IMF's and LCP's emitted from the intermediate velocity region (squares) and those emitted statistically (circles) as a function incident energy, for the four most peripheral Etrans12 bins. IMF's—solid symbols, LCP's—empty symbols. Lower row: probability that detected IMF (solid square) or LCP (empty square) comes from the mid-velocity region. The results are for method I.

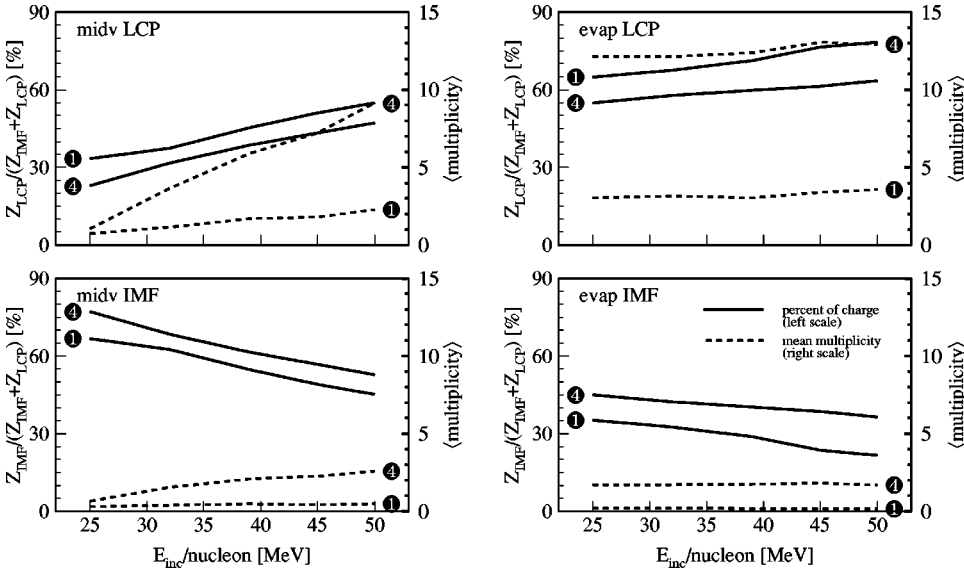


FIG. 6. Composition of midvelocity (left column) and statistical (right column) components for bins 1 and 4 as a function of incident energy. Solid lines referring to left scales represent the percentage of IMF's or LCP's in a given component, and dashed lines referring to right scales show mean multiplicities of these products. The results are for method I.

multiplicities of the midvelocity LCP's and IMF's (squares) increase significantly when passing from 25 to 50 MeV/nucleon incident energy.

The total (sum of midvelocity and evaporative contributions) IMF multiplicity is seen to be slowly increasing as a function of the incident energy for the more peripheral reactions. This appears to agree with similar measurements made by Peaslee *et al.* [18].

The competition between the evaporative and midvelocity emissions of the IMF's (circles and squares connected by a solid line) is also interesting to notice. Starting from 32 MeV/nucleon incident energy, for all four impact parameter bins, the mean multiplicity of IMF's originating from the midvelocity region is greater than or comparable to the mean multiplicity of the evaporated IMF's. Taking into account the fact that the first four bins exhaust about 80% of the total measured cross section and that the mean multiplicity of the midvelocity IMF's reaches up to two IMF's per event for 50 MeV/nucleon incident energy, we may draw the conclusion that the midvelocity emissions constitute a *very important* and efficient source of IMF's for peripheral and midcentral collisions in the Fermi energy domain.

The lower row in Fig. 5 presents the probability that the detected IMF (solid line) or LCP (dashed line) originates from the midvelocity region. As can be seen this probability reaches up to 60–75 % for IMF's from the four first bins. As far as the LCP's are concerned (dashed line) the midvelocity source is less competitive: only up to 40% of the detected LCP's originate from the midvelocity source at the highest energy.

Figure 6 summarizes, for bin 1 and 4, some of this information by showing, on the left axis, the percentage of the sum of the charge of LCP's (IMF's) coming from either mechanisms. The right axis of Fig. 6 shows the corresponding mean multiplicities. The evolution of the percentage of the sum of charge of IMF's in the midvelocity region which decreases from 75 to 50 % is one of the more remarkable features. These figures indicate that at lower incident energies, the midvelocity component is relatively smaller and more likely to be composed of IMF's. At higher energies the

midvelocity component is more fragmented and is composed of both IMF's and LCP's.

Figure 7 takes a closer look at the nature of the midvelocity and evaporative emissions. It presents the atomic number distributions for these two sources for four of the most peripheral impact parameter bins. These spectra are constructed in the following way: the evaporative and the total (forward

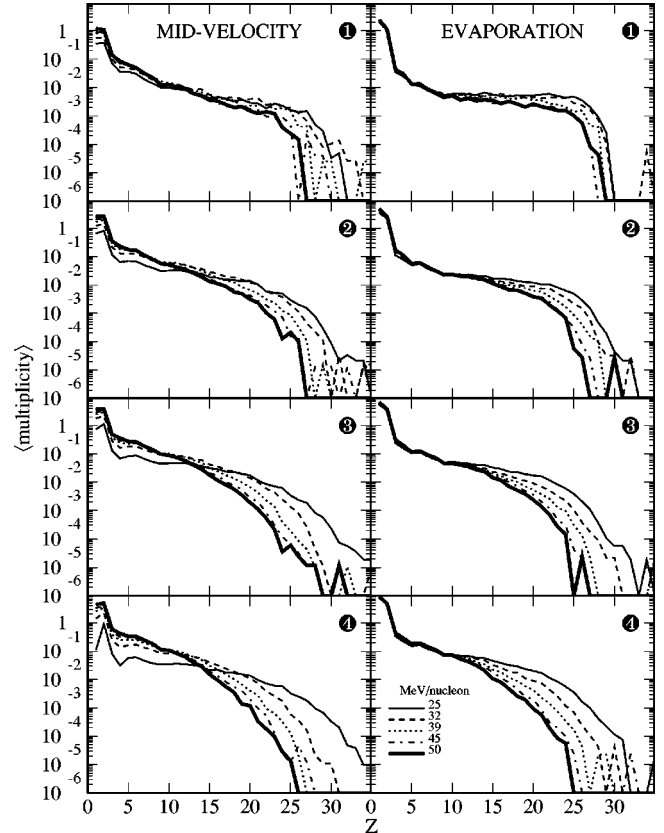


FIG. 7. Z distributions for midvelocity (left column) and statistical (right column) components for bins 1 to 4, for all incident energies (see legend). The heaviest fragment is excluded from the distributions. The results are for method I.

hemisphere)  $Z$  distributions are constructed for each bin in Etrans12. The former is then doubled and subsequently subtracted from the latter to obtain the midvelocity  $Z$  distribution. This distribution is therefore dependent on this subtraction and because of fluctuations, it can eventually contain negative probabilities.

There are three features that stand out in these figures: the extension of the  $Z$  distribution of the midvelocity distribution, the limited  $Z=1$  yield, particularly at the lower incident energies, and the independence of the lower part ( $Z \leq 10$ ) of the  $Z$  distribution of the evaporative component with incident energy.

The singular extension, up to  $Z=30$ , of the midvelocity component is explained by the variety of mechanisms that populate it and by the subtraction method used to construct the left panels of Fig. 7. The case of symmetric fission can be used to illustrate the limits of the subtraction method. In this case, one of the fission fragments will have a velocity smaller than the average  $Z_{\max}$  velocity (for this particular impact parameter bin). If it is not the heaviest fragment in the event, there is a certain probability that the subtraction method will assign it as a midvelocity product.

Besides symmetric fission, one of the mechanisms that populate the midvelocity region is *fast oriented fission* [3]. This corresponds to scenarios where the quasiprojectile is strongly deformed and emits this, possibly large, deformation towards the target direction (see Fig. 7 from Ref. [8] for an illustration of this process). This process is distinguished from fission by the fact that the angular distribution of the fragments is strongly peaked along the direction between the quasiprojectile and quasitarget. Notice that these fragments will be accounted for in the midvelocity component by both methods I and II as long as they do not represent the heaviest fragment in the forward hemisphere. This still leaves room for very heavy fragments in the case of quasisymmetric fission. The fact that these fragments can exceed  $Z$  values of half the projectile charge is due to fluctuations in the total charge collected in this forward hemisphere [19,20]. Thus the large extension of midvelocity  $Z$  values should be interpreted cautiously and should take into consideration the fluctuations that the subtraction method is unable to remove.

The small number of light fragments ( $Z \leq 15$ ) at 25 and 32 MeV/nucleon for bins 3 and 4 is due to the fact that the difference method used to construct these midvelocity distributions suffers when the mean velocity becomes close to the center-of-mass velocity. This effect is already seen in Figs. 3 and 4 when the total size of this component becomes negative. Nevertheless the fact remains that, compared to other species, light fragments seem to be less probable at these incident energies (see Fig. 5).

The study of the evaporative component shows, once again, the remarkable constancy, for a given impact parameter bin, of this component as a function of incident energy. Except for the heavier ions ( $Z \geq 10$ ), the  $Z$  distributions are almost indistinguishable. There is however a clear dependence on the impact parameter bin. Both of these points will be addressed in the next section.

The chemical composition of the midvelocity and evaporative components is examined in more details in Fig. 8. This

figure presents the multiplicities of  $p$ ,  $d$ ,  $t$ ,  ${}^3\text{He}$ ,  $\alpha$ ,  ${}^6\text{Li}$ , and  ${}^7\text{Li}$  for midvelocity (solid circle) and evaporative (empty circle) components, for the four largest impact parameter bins and for all incident energies. A general feature emerging from this figure is the increasing multiplicity of midvelocity particles with the increasing mass of the isotope for a given species. For each incident energy and species presented in the figure midvelocity emissions favor the more neutron rich isotopes. Especially interesting are the tritons which, beyond 32 MeV/nucleon, are more likely to be produced dynamically than statistically. Thus one can state that tritons appear to be *typical midvelocity particles* [17]. For example, at 50 MeV/nucleon, 60–70% of the tritons are produced in the midvelocity region. As stated before, protons show the opposite feature, since especially at lower beam energies, they are much more likely to originate from the evaporative processes than from dynamical emissions.

If one calculates the ratio of neutrons bound in  $Z=1-3$  elements (including the proton themselves) with respect to the number of protons bound in the same elements, one obtains values of 1.05 for the midvelocity region and 0.70 for the evaporative region. These numbers are almost independent of the incident energy and of the impact parameter bin number.

## VI. COMPARISON WITH MODEL PREDICTIONS

In a previous paper [8] the experimental results were compared to the predictions of two dynamical models: the stochastic mean field and the Landau Vlasov models. In this paper we test the predictive power of another model originating from the molecular dynamics family. This model, or strictly speaking its numerical implementation (CHIMERA [21]: Code for Heavy Ion Medium Energy ReActions) is a compilation of two molecular dynamics models, i.e., the quasiparticle dynamics (QPD) model of Boal and Glosli [22,23] and the quantum molecular dynamics (QMD) model of Aichelin and Stöcker [24–27]. In principle these two models are very similar. The main difference between them is in the preparation of the initial configurations and in the nucleon-nucleon potentials used.

A thorough theoretical background of the QMD model including derivation of the QMD equation and the necessary approximations can be found in a review article of Aichelin [26]. A detailed description of CHIMERA, as well as some of its predictions, are presented in Refs. [21,28,29], and here we only briefly present its main characteristics.

(1) Each nucleon (quasiparticle) is represented by a constant width minimal wave packet (coherent state).

(2) The  $N$ -body “wave function,” describing the entire nucleus is taken to be a direct product of  $N$  single particle states. This, of course, is a violation of the antisymmetry rules. Here it is assumed that the fermionic effects, which are believed to be essential for a reasonable treatment of the dynamics, can be simulated with the use of an effective potential term (Pauli potential) and with Pauli blocking of final states of individual nucleon-nucleon collisions. The Pauli potential plays also an important role during initialization of cold nuclei. It prevents the nucleons of the same kind from

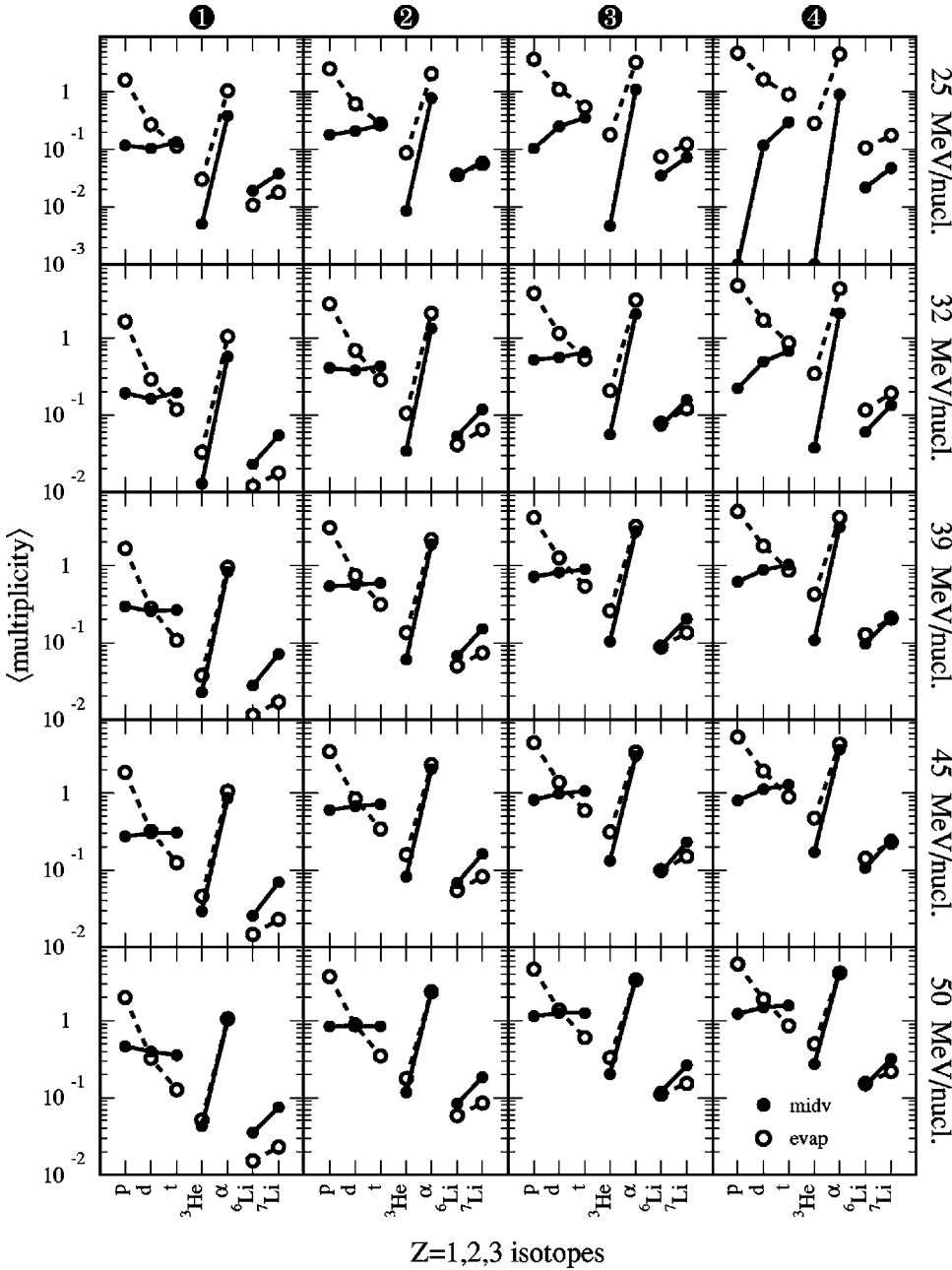


FIG. 8. Mean multiplicities of H, He, and Li isotopes for midvelocity (solid circles) and statistical (empty circles) components for bins 1–4 and for all incident energies. The results are for method I.

being too close in phase space.

(3) The time evolution of the  $N$ -body “wave function” describing the entire system is assumed to be governed by appropriate variational principle [26–30]. For the presumed “wave function” this evolution reduces simply to the classical Hamilton equations of motion for the centroids of the Gaussian wave packets. Thus the mean positions and momenta of  $N$  nucleons are assumed to evolve due to mutual two- and three-body effective nucleon-nucleon interactions along classical trajectory in phase space.

(4) The influence of the scattering term on the time evolution of the system is simulated by a Monte Carlo procedure (see, e.g., [31]). Whenever two nucleons come closer than the distance determined by a free, energy dependent [32], nucleon-nucleon cross section, they are assumed to scatter isotropically (with the angular momentum being conserved

“on average”), provided the final states are not occupied. The occupancy of phase space around the presumed final state of the scattered nucleon is assumed to be the overlap of the phase space distribution of the scattered nucleon in its presumed final state, with the phase space distributions of all the remaining nucleons.

(5) The Hamiltonian utilized in the CHIMERA code has the same functional form as that used in the model of Boal and Glosli [22], including all the terms of nuclear potential as well as Pauli and Coulomb terms. We use two sets of parameters of the potential in order to vary the stiffness of the corresponding nuclear matter equation of state (EOS). These two sets lead to soft and hard EOS, with the incompressibility constants  $K \approx 200$  and 350 MeV, respectively. The values of the parameters can be found in [21]. The model reproduces very well the bulk static properties, such as binding

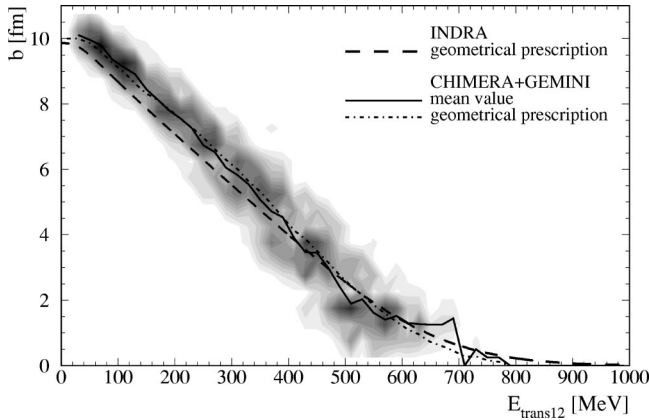


FIG. 9. Relationship between  $E_{\text{trans12}}$  and impact parameter for 50 MeV/nucleon Xe+Sn. Gray level contour plot represents the results of the CHIMERA+GEMINI calculation, the solid line represents its mean value, and the dashed-dotted line represents the result of a geometrical prescription applied to the simulation. The dashed line represents the result of a geometrical prescription applied to experimental data (see Sec. III and Fig. 2).

energies or rms radii, especially for heavier nuclei for which the local density approximation is the best.

(6) The ground-state configurations of the nuclei were found by solving a set of damped equations of motion.

(7) Initial conditions of nuclear collisions were set by assuming that the colliding ions move along classical Coulomb trajectories until the distance between their surfaces is 3 fm.

(8) After a specified time the dynamical evolution is stopped. All nucleons which are separated in the configuration space by less than 3 fm are assumed to form a cluster. Each cluster is then assigned a mass number, atomic number, c.m. position, linear momentum, binding energy, temperature, and spin. The binding energy allows for later determination of the excitation energy.

(9) In order to make direct comparison with the experi-

mental data, after stopping the dynamical evolution, the decay chains of the excited fragments are calculated with the use of the statistical code GEMINI [33].

Such simulations are impact parameter dependent and Fig. 9 shows the predictions of the model for the relationship between the impact parameter and  $E_{\text{trans12}}$  for 50 MeV/nucleon incident energy. As can be seen these two quantities are indeed very well correlated. The solid line in this figure represents the mean value of the contour plot, and the dash-dotted line represents the result of the geometrical prescription, (see Sec. III), applied to the model  $E_{\text{trans12}}$  spectrum (see Fig. 2). The good agreement between the histogram and the mean value seems to justify, within this model, the use of the geometrical prescription for finding the relationship between the impact parameter and the  $E_{\text{trans12}}$  observable. Finally, the dashed line depicted in this figure represents (see also Fig. 2) the experimental result of the geometrical prescription applied to the  $E_{\text{trans12}}$  spectrum. The agreement between the INDRA results and the model prediction is very encouraging. The quantitative model reproduction of the range of  $E_{\text{trans12}}$  values is also a feature that should be pointed out. At lower energies (i.e., at 25 MeV/nucleon, where the model is not supposed to work as well) the agreement is not as good, but does not rule out the use of this approximation for the most peripheral reactions.

In the following analysis of the simulated data, the same methods have been used as those for the experimental data and the  $E_{\text{trans12}}$  parameter is used as the sorting parameter. Figure 10 presents the results of the model as was done for the data in Fig. 3. Panel (a) presents the percentage of charge contained in the midvelocity and evaporative components as a function of  $E_{\text{trans12}}$  for method I. The qualitative agreement is clear and in particular the onset at low energy is present. The quantitative comparison shows that midvelocity emissions are however underestimated by about 40%. It has to be stressed here, that these results are obtained using the soft EOS parameters. The use of the hard equation of state

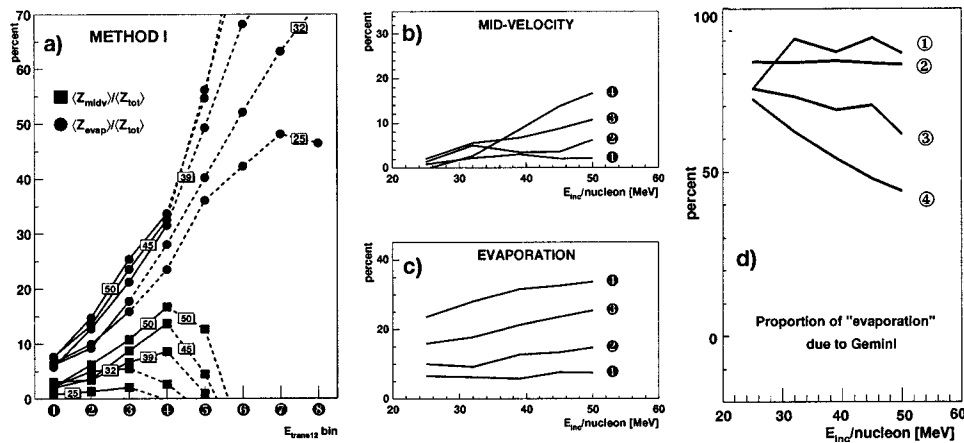


FIG. 10. Model equivalent of Fig. 3. (a) The percentage of charge emitted in the forward hemiellipsoid of momentum tensor for midvelocity emissions (squares) and evaporation processes (circles) obtained with method I as a function of  $E_{\text{trans12}}$  and for soft EOS.  $Z_{\text{tot}} = Z_{\text{midv}} + Z_{\text{evap}} + Z_{\text{heaviest}}$ . The numbers in boxes label the incident energies. The dashed lines specify the impact parameter region for which the subtraction method gives unreliable results. (b) The percentage of charge in midvelocity component as a function of incident energy for the four lowest  $E_{\text{trans12}}$  bins. (c) Same as (b) but for statistical emission. (d) The percentage of the evaporative component that is due to the GEMINI afterburner. White circles with numbers denote impact parameter bins defined in Fig. 2.

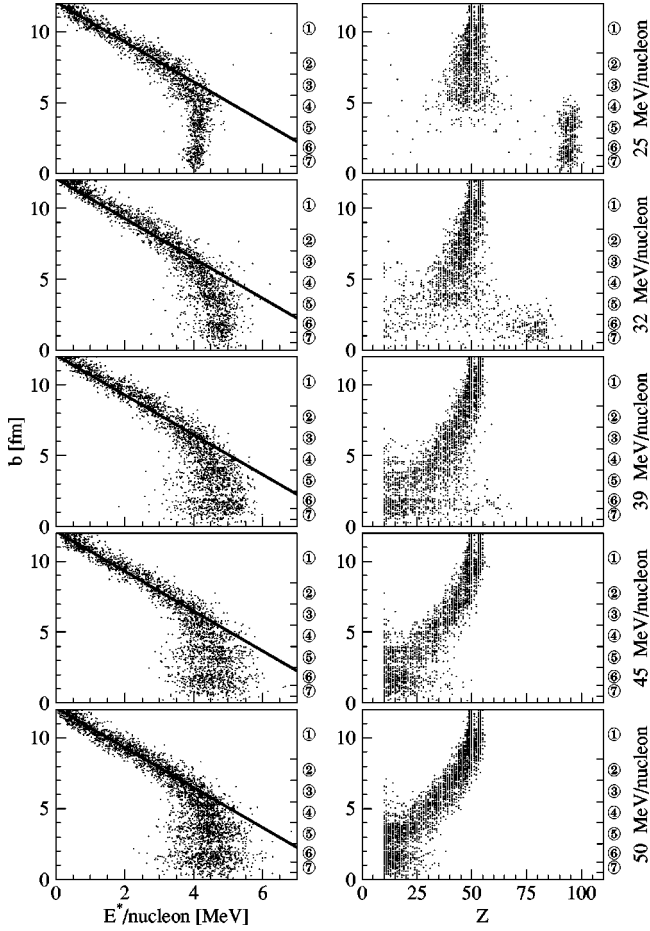


FIG. 11. Left column: impact parameter dependence of excitation energies per nucleon for fragments with  $Z \geq 10$ , for all incident energies. Right column: relation between impact parameter and atomic number of a fragment. Right scales show the impact parameter binning (cf. Fig. 2). The results of CHIMERA calculation after 600 fm/c.

gives a further reduction of the midvelocity component (by more than a factor of 4). If confirmed, this interesting feature could be used to distinguish between different equations of state. In fact, this component is formed mainly in the early, dynamical phase of the reaction, during which compression and decompression effects could be important. Similar preferences for a soft EOS can be found also in Refs. [6,29,34].

Another interesting observation follows from panel (c) of Fig. 10. The model reproduces the experimentally observed constancy of the evaporated charge as a function of incident energy, at least for the two most peripheral impact parameter bins [see also Figs. 3 and 4(c)]. This observation might at first glance suggest the invariance of the excitation energy per nucleon of the primary source, on the incident energy and for a given impact parameter bin. In order to verify this hypothesis we have plotted in Fig. 11 the correspondence between the impact parameter and the excitation energies per nucleon of the fragments with  $Z \geq 10$  (left column), and the correspondence between the impact parameter and the  $Z$  number of the emitted fragments (right column), after 600 fm/c, and for all incident energies. Here one comment is

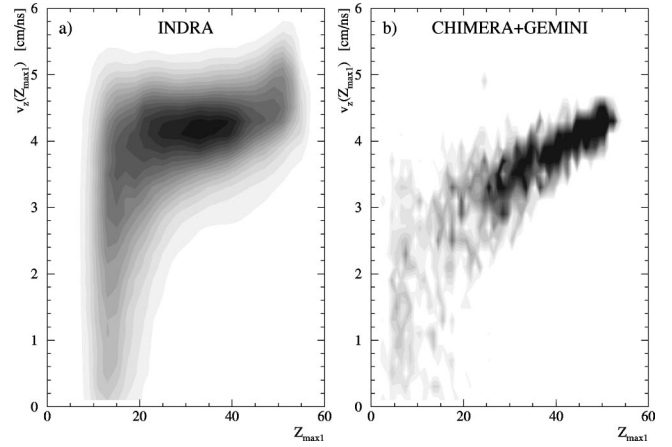


FIG. 12. Velocity component of the heaviest fragment along the main ellipsoid axis as a function of atomic number of this fragment for 50 MeV/nucleon Xe+Sn. (a) Experimental result, (b) CHIMERA+GEMINI.

needed: the CHIMERA model predicts rather slow statistical emission rates, thus even after 600 fm/c, at least for more peripheral collisions, the observed fragments are still “good” prefragments excited up to 4–5 MeV/nucleon. Thus the need for an afterburner is obvious. Nevertheless, after 600 fm/c the dynamical phase can be regarded as over. Figure 10(d) shows, in percentage, that the evaporative component is largely due to the GEMINI afterburner. The choice of 600 fm/c is not critical and represents only a compromise between computation time and the strength of the Coulomb forces which are neglected once the GEMINI code is used. Calculations that were stopped at 300 fm/c showed that the effect of this stopping time was negligible.

Also in Fig. 11, the lines (identical for all panels) in the left column show that indeed the excitation energy per nucleon of the excited prefragments does not depend on the incident energy but only on the impact parameter. The right column of this figure shows two interesting features. First, at 25 and 32 MeV/nucleon a composite system is formed at small impact parameters; evidently this system survives at least up to 600 fm/c. For energies above 32 MeV/nucleon, such a system is not seen. This can either be interpreted as the disappearance of these processes or as the fact that a fast (at least faster than 600 fm/c) multifragmentation process occurs. Such aspects go beyond the scope of this paper.

More relevant to the present problem is the observation that the charges of heavy fragments decrease both with increasing incident energy and with decreasing impact parameter. This is related to the appearance of the midvelocity component. This is not an effect due to the finite time limit (600 fm/c) of the calculation since at 25 MeV/nucleon a constancy of the quasiprojectile (target) size is observed.

Figure 12 compares the velocity of the heaviest fragments as measured by INDRA [Fig. 12(a)] and as predicted by the model [Fig. 12(b)]. The experimental data show that very little velocity damping is observed whereas the model predicts a more important one. This is an interesting feature since other dynamical codes [24,35] give different predictions. This overestimation of the velocity damping could be

related to the observed underprediction of the magnitude of midvelocity emissions (see Fig. 10) and shows that these emissions could be, in fact, sensitive both to the finer ingredients of these dynamical codes and to the proper treatment of Pauli-blocking and related transparency effects.

## VII. SUMMARY AND CONCLUSION

The analysis performed in this paper is an extension of a previous one [8], carried out for Xe+Sn at 50 MeV/nucleon only. This extended analysis, for the Xe+Sn reaction at 25, 32, 39, 45, and 50 MeV/nucleon is again performed as a function of transverse energy of light charged particles. This enabled us to study the evolution of various observables as a function of impact parameter. The analysis shows the following features.

First, at 25 MeV/nucleon the dynamical effects are small. The extracted midvelocity component lies below 12% of the total charge for intermediate impact parameter collisions. This contribution of midvelocity charge, for the same impact parameter range, rises with incident energy up to 18–30% for 50 MeV/nucleon. This may lead us to the conclusion that, on entering the Fermi energy domain, we encounter the onset of the midvelocity emissions.

At the highest incident energy, the amount of midvelocity charge approaches the geometrical overlap of the projectile and the target. This observation may indicate that, in fact, at 50 MeV/nucleon the reaction picture starts to resemble the high energy participant-spectator scenario, although it is clear that, at these energies, the origin of the midvelocity component is far more complex than that of the simple fire-ball model.

Second, investigation of the evaporative component of the particles and fragments shows that the amount of evaporated charge for a given impact parameter range almost does not depend on the incident energy, for peripheral and midcentral collisions. Thus, midvelocity emission constitutes the main difference in emission pattern for the incident energies studied. Invariance of the evaporated charge of the incident energy for the same impact parameters may imply the same excitation energy per nucleon of the corresponding sources of this evaporated charge for a given impact parameter. The constancy of this *evaporative* component coupled to the in-

crease of the *midvelocity* is an intriguing feature which has to be understood.

A third observation concerns the evolution of the composition of the midvelocity component with the incident energy. The analysis shows that the midvelocity component is more likely to be composed of IMF's at lower energies (up to 75% of the charge of this component comes from IMF's) than at higher ones (about 50%). On the contrary, the contribution of protons to midvelocity emissions increases with the incident energy. Alpha particles contribute 40% to the midvelocity component, independently of incident energy. This may result from the more violent nature of the collisions in the participant region as the incident energy increases.

Fourth, the isotopic composition of the midvelocity component clearly shows that this component favors neutron rich isotopes. For peripheral collisions and lower energies the midvelocity component is more likely to be composed of tritons and deuterons than of protons. At 50 MeV/nucleon mean multiplicities of these isotopes are equal.

Comparisons of the experimental data with the QPD/QMD+GEMINI calculations performed for the reactions considered, show a qualitative agreement with the experimental data. The incident energy dependence, and in particular the onset of midvelocity emissions is reproduced. The differences observed both in the quantitative comparison as well as in the quasiprojectile velocity damping show that these phenomenon could be sensitive to the finer details of such dynamical models. In particular the reproduction of the neutron richness of the neck component and the relative abundance of the light particles could be a task for the next generation of dynamical models (AMD [36], FMD [37]) which would take into account finer quantum effects. This is beyond the possibilities of the CHIMERA code used in this analysis.

## ACKNOWLEDGMENTS

The work was supported in part by the agreement between IN2P3 and Polish Laboratories, under Grant No. 98-91. The model simulations were performed on the SPP1600/XA computer at the ACK CYFRONET, Kraków.

- 
- [1] J. Randrup, Nucl. Phys. **A383**, 468 (1983).  
 [2] L. Stuttgé, J.C. Adloff, B. Bilwes, R. Bilwes, F. Cosmo, M. Glaser, G. Rudolf, F. Scheibling, R. Bougalut, J. Colin, F. Delaunay, A. Genoux-Lubain, D. Horn, C. Le Brun, J.F. Lecolley, M. Louvel, J.C. Steckmeyer, and J.L. Ferrero, Nucl. Phys. **A539**, 511 (1992).  
 [3] G. Casini, P.G. Bizzeti, P.R. Maurenzig, A. Olmi, A.A. Stefanini, J.P. Wessels, R.J. Charity, R. Freifelder, A. Gobbi, N. Herrmann, K.D. Hildenbrand, and H. Stelzer, Phys. Rev. Lett. **71**, 2567 (1993).  
 [4] C.P. Montoya, W.G. Lynch, D.R. Bowman, G.F. Peaslee, N. Carlin, R.T. de Souza, C.K. Gelbke, W.G. Gong, Y.D. Kim, M.A. Lisa, L. Phair, M.B. Tsang, J.B. Webster, C. Williams, N. Colonna, K. Hanold, M.A. McMahan, G.J. Wozniak, and L.G. Moretto, Phys. Rev. Lett. **73**, 3070 (1994).  
 [5] J.F. Lecolley, L. Stuttgé, M. Aboufirassi, B. Bilwes, R. Bougault, R. Brou, F. Cosmo, J. Colin, D. Durand, J. Galin, A. Genoux-Lubain, D. Guerreau, D. Horn, D. Jacquet, J.L. Laville, F. Lefebvres, C. Le Brun, O. Lopez, M. Louvel, M. Mahi, C. Meslin, M. Morjean, A. Péghaire, G. Rudolf, F. Scheibling, J.C. Steckmeyer, B. Tamain, and S. Tomasevic, Phys. Lett. B **354**, 202 (1995).  
 [6] J.F. Dempsey, R.J. Charity, L.G. Sobotka, G.J. Kunde, S. Gaff, C.K. Gelbke, T. Glasmacher, M.J. Huang, R.C. Lemmon, W.G. Lynch, L. Manduci, L. Martin, M.B. Tsang, D.K. Agnihotri, B. Djerroud, W.U. Schröder, W. Skulski, J. Töke, and

- W.A. Friedman, *Phys. Rev. C* **54**, 1710 (1996).
- [7] Y. Larochelle, L. Gingras, L. Beaulieu, X. Qian, Z. Saddiki, B. Djerroud, D. Dore, R. Laforest, R. Roy, K. Samri, C. St-Pierre, G. C. Ball, D. R. Bowman, A. Galindo-Uribarri, E. Hagberg, D. Horn, J. A. Lopez, and T. Robinson, *Phys. Rev. C* **55**, 1869 (1997); Y. Larochelle, L. Gingras, L. Beaulieu, R. Laforest, R. Roy, K. Samri, C. St-Pierre, *ibid.* **57**, R1027 (1998); Y. Larochelle, C. St-Pierre, L. Beaulieu, N. Colonna, L. Gingras, G. C. Ball, D. R. Bowman, M. Colonna, G. D'Erasmus, E. Fiore, D. Fox, A. Galindo-Uribarri, E. Hagberg, D. Horn, R. Laforest, A. Pantaleo, R. Roy, and G. Tagliente, *ibid.* **59**, R565 (1999).
- [8] J. Łukasik, J. Benlliure, V. Métivier, E. Plagnol, B. Tamain, M. Assenard, G. Auger, Ch.O. Bacri, E. Bisquer, B. Borderie, R. Bougault, R. Brou, Ph. Buchet, J.L. Charvet, A. Chbihi, J. Colin, D. Cussol, R. Dayras, A. Demeyer, D. Doré, D. Durand, E. Gerlic, S. Germain, D. Gourio, D. Guinet, P. Loutesse, J.L. Laville, J.F. Lecomte, A. Le Fèvre, T. Lefort, R. Legrain, O. Lopez, M. Louvel, N. Marie, L. Nalpas, M. Parlog, J. Péter, O. Politi, A. Rahmani, T. Reposeur, M.F. Rivet, E. Rosato, F. Saint-Laurent, M. Squalli, J.C. Steckmeyer, M. Stern, L. Tassan-Got, E. Vient, C. Volant, J.P. Wieleczko, M. Colonna, F. Haddad, Ph. Eudes, T. Sami, and F. Sebillé, *Phys. Rev. C* **55**, 1906 (1997).
- [9] J. Péter, S.C. Jeong, J.C. Angélique, G. Auger, G. Bizard, R. Brou, A. Buta, C. Cabot, Y. Cassagnou, E. Crema, D. Cussol, D. Durand, Y. El Masri, P. Eudes, Z.Y. He, A. Kerambrun, C. Lebrun, R. Legrain, J.P. Patry, A. Péghaire, R. Régimbart, E. Rosato, F. Saint-Laurent, J.C. Steckmeyer, B. Tamain, and E. Vient, *Nucl. Phys. A* **593**, 95 (1995).
- [10] P. Pawłowski, J. Brzychczyk, A.J. Cole, P. Désesquelles, W. Gawlikowicz, K. Grotowski, P. Hachaj, S. Micek, R. Płaneta, Z. Sosin, A. Wieloch, D. Benchekekroun, E. Bisquer, A. Chabane, A. Demeyer, M. Charvet, B. Cheynis, E. Gerlic, A. Giorni, D. Guinet, D. Heuer, P. Loutesse, L. Lebreton, A. Llères, M. Stern, L. Vagneron, and J.B. Viano, *Phys. Rev. C* **57**, 1771 (1998).
- [11] J. Pouthas, B. Borderie, R. Dayras, E. Plagnol, M.F. Rivet, F. Saint-Laurent, J.C. Steckmeyer, G. Auger, C.O. Bacri, S. Barbey, A. Barbier, A. Benkirane, J. Benlliure, B. Berthier, E. Bougamont, P. Bourgault, P. Box, R. Bzyl, B. Cahan, Y. Cassagnou, D. Charlet, J.L. Charvet, A. Chbihi, T. Clerc, N. Copinet, D. Cussol, M. Engrand, J.M. Gautier, Y. Hugué, O. Journaux, J.L. Laville, P. Le Botlan, A. Leconte, R. Legrain, P. Lelong, M. Le Guay, L. Martina, C. Mazur, P. Mosrin, L. Olivier, J.P. Passerieux, S. Pierre, B. Piquet, E. Plaige, E.C. Pollacco, B. Raine, A. Richard, J. Ropert, C. Spitaels, L. Stab, D. Sznajderman, L. Tassan-Got, J. Tillier, M. Tripon, P. Vallerand, C. Volant, P. Volkov, J.P. Wieleczko, and G. Wittwer, *Nucl. Instrum. Methods Phys. Res. A* **357**, 418 (1995); J. Pouthas, A. Bertraut, B. Borderie, P. Bourgault, B. Cahan, G. Carles, D. Charlet, D. Cussol, R. Dayras, M. Engrand, O. Journaux, P. LeBotlan, A. Leconte, P. Lelong, L. Martina, P. Mosrin, L. Olivier, J.P. Passerieux, B. Piquet, E. Plagnol, E. Plaige, B. Raine, A. Richard, F. Saint-Laurent, C. Spitaels, J. Tillier, M. Tripon, P. Vallerand, P. Volkov, and G. Wittwer, *ibid.* **369**, 222 (1996); J.C. Steckmeyer *et al.*, *ibid.* **361**, 472 (1995).
- [12] C. Cavata, M. Demoulin, J. Gosset, M-C. Lemaire, D.D. L'Hôte, J. Poitou, and O. Valette, *Phys. Rev. C* **42**, 1760 (1990).
- [13] J. Cugnon and D. L'Hôte, *Nucl. Phys. A* **397**, 519 (1983).
- [14] V. Métivier, B. Tamain, G. Auger, C.O. Bacri, A. Benkirane, J. Benlliure, B. Berthier, B. Borderie, R. Bougalut, P. Box, R. Brou, Y. Cassagnou, J.L. Charvet, A. Chbihi, J. Colin, D. Cussol, R. Dayras, E. De Filippo, A. Demeyer, D. Durand, P. Ecomard, P. Eudes, A. Genoux-Lubain, D. Gourio, D. Guinet, R. Laforest, L. Lakehal-Ayat, P. Loutesse, J.L. Laville, L. Lebreton, C. Le Brun, J.F. Lecomte, A. Le Fèvre, R. Legrain, O. Lopez, M. Louvel, M. Mahi, N. Marie, T. Nakagawa, L. Nalpas, A. Ouattizerga, M. Parlog, J. Péter, E. Plagnol, E. Pollacco, A. Rahmani, R. Régimbart, T. Reposeur, M.F. Rivet, E. Rosato, F. Saint-Laurent, M. Squalli, J.C. Steckmeyer, L. Tassan-Got, E. Vient, C. Volant, J.P. Wieleczko, A. Wieloch, and K. Yusa-Nakagawa, *Proceedings of the ACS Nuclear Chem Symposium, Anaheim, CA, 1995*.
- [15] Ph. Eudes, Z. Basrak, and F. Sebillé, *Phys. Rev. C* **56**, 2003 (1997).
- [16] K. Summerer, W. Bruchle, D.J. Morrissey, M. Schadel, B. Szweryn, and Yang Weifan, *Phys. Rev. C* **42**, 2546 (1990).
- [17] T. Lefort *et al.*, LPC (Caen, France) Preprint LPCC 98-15, submitted to *Nucl. Phys. A*.
- [18] G.F. Peaslee, in *Proceedings of the XXXI International Winter Meeting on Nuclear Physics*, Bormio (Italy), 1993, edited by I. Iori (Ricerca Scientifica ed Educazione Permanente, Supplemento No. 96, 1993), p. 1; G.F. Peaslee, M.B. Tsang, C. Schwarz, M.J. Huang, W.S. Huang, W.C. Hsi, C. Williams, W.W. Bauer, D.R. Bowman, M. Chartier, J. Dinius, C.K. Gelbke, T. Glasmacher, D.O. Handzy, M.A. Lisa, W.G. Lynch, C.M. Mader, L. Phair, M-C. Lemaire, S.R. Souza, G. Van Buren, R.J. Charity, L.G. Sobotka, G.J. Kunde, U. Lynen, J. Pochodzalla, H. Sann, W. Trautmann, D.D. Fox, R.T. Souza, G. Peilert, W.A. Friedman, and C. Carlin, *Phys. Rev. C* **49**, R2271 (1994).
- [19] F. Bocage, University thesis, University of Caen, France, 1998.
- [20] J. Colin *et al.*, *Nucl. Phys. A* **593**, 48 (1995); J. Colin, Habilitation thesis, University of Caen, France, 1998.
- [21] J. Łukasik and Z. Majka, *Acta Phys. Pol. B* **24**, 1959 (1993); J. Łukasik, Ph.D. thesis, Kraków, 1993.
- [22] D.H. Boal and J.N. Gosli, *Phys. Rev. C* **38**, 1870 (1988).
- [23] D.H. Boal and J.N. Gosli, *Phys. Rev. C* **38**, 2621 (1988); D.H. Boal, J.N. Gosli, and C. Wicentowich, *ibid.* **40**, 601 (1989); D.H. Boal and J.C.K. Wong, *ibid.* **41**, 118 (1990).
- [24] J. Aichelin and H. Stöcker, *Phys. Lett. B* **176**, 14 (1986); G. Peilert, H. Stöcker, W. Greiner, A. Rosenhauer, A. Bohnet, and J. Aichelin, *Phys. Rev. C* **39**, 1402 (1989); G. Peilert, J. Aichelin, H. Stöcker, and W. Greiner, in *Nuclear Dynamics and Nuclear Disassembly*, Proceedings of the Symposium, Dallas, Texas, 1989, edited by J.B. Natowitz (World Scientific, Singapore, 1989); A. Bohnet, N. Ohtsuka, J. Aichelin, R. Linden, and A. Faessler, *Nucl. Phys. A* **494**, 349 (1989); C. Hartnack, Li Zhuxia, L. Neise, G. Peilert, A. Rosenhauer, H. Sorge, J. Aichelin, H. Stöcker, and W. Greiner, *ibid.* **A495**, 303c (1989); L. Neise, M. Berenguer, C. Hartnack, G. Peilert, H. Stöcker, and W. Greiner, *ibid.* **A519**, 375c (1990); T. Maruyama, S.W. Huang, N. Ohtsuka, G. Li, A. Faessler, and J. Aichelin, *ibid.*, **A534**, 720 (1991); A. Bohnet, J. Aichelin, J. Pochodzalla, W. Trautmann, G. Peilert, H. Stöcker, and W. Greiner, *Phys. Rev. C* **44**, 2111 (1991); P. Valta, J. Konopka,

- M. Berenguer, A. Bohnet, J. Jaenicke, S. Huber, C. Hartnack, G. Peilert, L.W. Neise, J. Aichelin, H. Stöcker, and W. Greiner, Nucl. Phys. **A538**, 417c (1992); G. Peilert, J. Konopka, H. Stöcker, W. Greiner, M. Blann, and M.G. Mustafa, Phys. Rev. C **46**, 1457 (1992); W. Müller, M. Begemann-Blaich, and J. Aichelin, Phys. Lett. B **298**, 27 (1993).
- [25] J. Aichelin, G. Peilert, A. Bohnet, A. Rosenhauer, H. Stöcker, and W. Greiner, Phys. Rev. C **37**, 2451 (1988).
- [26] J. Aichelin, Phys. Rep. **202**, 233 (1991).
- [27] G. Peilert, J. Randrup, H. Stöcker, and W. Greiner, Phys. Lett. B **260**, 271 (1991).
- [28] J. Łukasik, Z. Majka, and T. Kozik, Phys. Lett. B **318**, 419 (1993); T. Kozik, V. Abenante, R.J. Charity, A. Chbihi, Z. Majka, N.G. Nicolis, D.G. Sarantites, L.G. Sobotka, D.W. Stracener, C. Baktash, M.L. Halbert, D.C. Hensley, and J. Łukasik, Phys. Rev. C **54**, 3088 (1996); J. Cibor, Z. Majka, T. Kozik, P. Staszal, Z. Sosin, K. Hagel, J. Li, L. Lou, R. Tezkratt, D. Utley, R. Wada, B. Xiao, and J.B. Natowitz *ibid.* **55**, 264 (1997).
- [29] J. Cibor, J. Łukasik, and Z. Majka, Z. Phys. A **348**, 233 (1994).
- [30] C. Cariano, R. Parwani, and H. Yamagishi, Nucl. Phys. **A552**, 591 (1991).
- [31] G.F. Bertsch and S. Das Gupta, Phys. Rep. **160**, 189 (1988).
- [32] K. Chen, Z. Fraenkel, G. Friedlander, J.R. Grover, J.M. Miller, and Y. Shimamoto, Phys. Rev. **166**, 949 (1968).
- [33] R.J. Charity, M.A. McMahan, G.J. Wozniak, R.J. McDonald, L.G. Moretto, D.G. Sarantites, L.G. Sobotka, G. Guarino, A. Pantaleo, L. Fiore, A. Gobbi, and K.D. Hildenbrand, Nucl. Phys. **A483**, 371 (1988); R.J. Charity, computer code GEMINI obtained from wunmr.wustl.edu via anonymous ftp.
- [34] V. de la Mota, F. Sébille, M. Farine, B. Remaud, and P. Schuck, Phys. Rev. C **46**, 677 (1992); F. Haddad, F. Sébille, M. Farine, V. de la Mota, P. Schuck, and B. Jouault, *ibid.* **52**, 2013 (1995).
- [35] O. Tirel, University thesis, University of Caen, France, 1998.
- [36] A. Ono, H. Horiuchi, T. Maruyama, and A. Ohnishi, Phys. Rev. Lett. **68**, 2898 (1992); Prog. Theor. Phys. **87**, 1185 (1992).
- [37] H. Feldmeier, Nucl. Phys. **A515**, 147 (1990).